NiFe$_2$O$_4$ Spinel Protection Coating for High-Temperature Solid Oxide Fuel Cell Interconnect Application

Reza Irankhah, Babak Raissi, Amir Maghsoudipour, Abdullah Irankhah, and Sasan Ghashghai

In the present study, Ni-Fe spinel powder was synthesized via a solid state reaction. In the next step, the electrophoretic deposition (EPD) method was used to apply the NiFe$_2$O$_4$ spinel, as an oxidation-resistant layer, on a commercially available stainless steel (SUS 430) in a potential range of 100 to 300 V. Microscopic studies of the deposited layers showed that crack-free NiFe$_2$O$_4$ films were obtained at 100 V. The coated and uncoated samples were then pre-sintered in air and 5% H$_2$ bal Ar atmospheres at 900 °C for 3 h followed by cyclic oxidation at 800 °C for 500 h. The investigation of the oxidation resistance of the samples using Energy Dispersive Spectroscopy (EDS) revealed that the NiFe$_2$O$_4$ coating acted as an effective barrier against chromium migration into the coating. The oxidation resistance of 5% H$_2$ bal Ar pre-sintered sample was enhanced with an oxidation rate constant (K_P) of 8.9×10^{-15} g^2 cm^{-4} s^{-1}.

Keywords	cyclic oxidation, electrophoretic deposition, NiFe$_2$O$_4$ Spinel, SOFC interconnect, solid state reaction

1. Introduction

Fuel cells efficiently convert chemical energy to electricity in a silent and environmentally friendly way. Among the various kinds of fuel cells, solid oxide fuel cells (SOFCs) have the ability to attain an efficiency over 80% (Ref 1) by converting chemical energy of the fuel oxidation reaction directly into electrical energy because of their high operating temperature (Ref 2, 3). The typical SOFC single cell consists of two electrodes, i.e., a porous cathode (or air electrode) and a porous anode (or fuel electrode) separated by the electrolyte (Ref 2, 4-6). In order to get useful voltage and power output, cells must be connected in series via interconnects to form a stack (Ref 7, 8). Figure 1(a) illustrates a planar SOFC stack (Ref 9). In the structure of solid oxide fuel cell stacks, appropriate electrical connection between the anode of one cell and the cathode of the neighboring cell is of great technical importance. For this purpose and also for efficient prevention of contact between the reducing and oxidizing atmospheres, interconnects have been conventionally employed within the cell arrangement. Interconnects should also have good oxidation resistance, suitable thermal conductivity, and thermal expansion coefficients (TEC) matching those of electrodes and electrolyte (Ref 4-6). Ceramic and metallic interconnects are most commonly used in these applications. Lanthanum chromite (LaCrO$_3$) is the traditional ceramic material used for the SOFC interconnect for high-temperature applications (~1000 °C) (Ref 10). Although ceramic interconnects based on perovskite

structure of LaCrO$_3$ are employed, they face some challenges which includes manufacture problems and low electrical conductivity (Ref 10-12). Many studies have been carried out to reduce the working temperature of solid oxide fuel cells from 1000 °C to lower operating temperatures (600-800 °C). Lower operating temperatures would give us a chance to use metallic interconnects as highly oxidation-resistant alloys to replace ceramic ones (Ref 12-14). Almost all of the candidate alloys being considered for this application are chromia-forming alloys, which can form a protective Cr$_2$O$_3$ oxide layer on the alloy surface when oxidized. This dense Cr$_2$O$_3$ oxide layer not only offers oxidation resistance but also has acceptable electrical conductivity and stability (Ref 7). Among chromia-forming alloys, ferritic stainless steel (such as SUS 430, Crofer 22, E-Brite) has been used as SOFC interconnect due to its good thermal expansion, low cost, excellent formability, and excellent anti-oxidation performance (Ref 7, 15, 16). However, several issues potentially hinder their application, including increasing electrical resistance over time, unavoidable oxidation, and chromium evaporation (Ref 7, 17). Under SOFC operating temperatures, the use of ferritic stainless steel will result in Cr migration via Cr$_2$O$_3$ oxide layer into the porous cathode and will poison the SOFC cathode which leads to performance degradation (Ref 7, 13, 18-20). Chromium contamination of SOFC cathodes has been observed by several groups of researchers (Ref 17, 21-32). The vaporization of chromium is based on the vaporization of Cr$_2$O$_3$ from the interconnect surface as CrO$_3$ or CrO$_2$(OH)$_2$ as major gaseous species. Chromium-containing vapor species formed from the interconnect material will electrochemically or chemically be reduced at the three-phase boundary [electrolyte/cathode/oxidant]. The resulting deposition can block the active electrode surface and degrade cell performance (Ref 11, 18). To avoid this damaging effect, conductive spinel coatings (Ref 7) such as (Cu,Mn)$_3$O$_4$ (Ref 33), (Mn,Co)$_3$O$_4$ (Ref 33, 34), Ni-Co (Ref 35), and Ni-Fe (Ref 36) spinels have been considered. (Ni, Fe)$_3$O$_4$ spinel exhibited high electrical conductivity, CTE match with other cell components and effective Cr retention (Ref 37). Although different methods such as screen printing (Ref 36), electroplating (Ref 36, 37), and magnetron sputtering (Ref 38) have been commonly used to
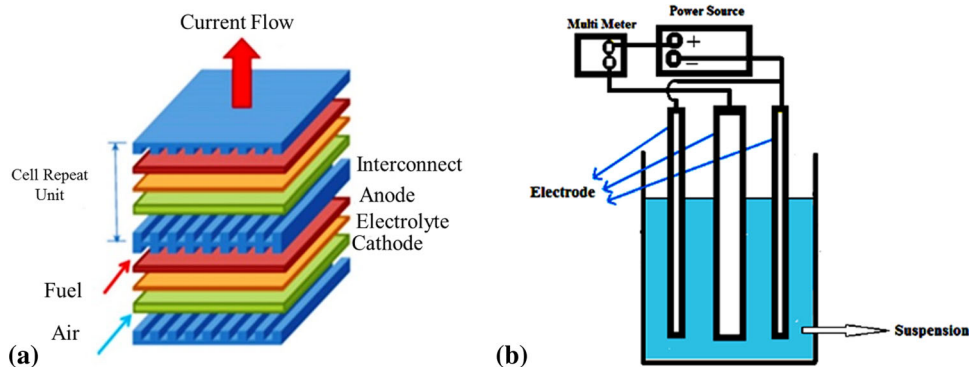
Reza Irankhah, Babak Raissi, Amir Maghsoudipour, and **Sasan Ghashghai**, Department of Ceramic, Materials and Energy Research Center, Tehran 14155-4777, Iran; and **Abdullah Irankhah**, Hydrogen and Fuel Cell Research Lab, Chemical Engineering Department, University of Kashan, Kashan 87317-51167, Iran. Contact e-mail: r.irankhah@gmail.com.

apply spinel coatings on the surface of metallic interconnects, the electrophoretic deposition (EPD) has recently attracted much attention in the application of ceramic layers of different thicknesses. In this process, ceramic particles dispersed in a liquid medium will migrate under a DC electric field toward the opposite electrode where they finally deposit, forming a thick layer on the surface (Ref 39). The EPD technique has advantages such as short formation time, easy control of the layer thickness, and morphology along with no needs for complex apparatus (Ref 40). In the present study, the EPD method is employed to deposit $NiFe_2O_4$ spinel particles on SUS 430 SOFC interconnect. The optimum electric field strength to form a crack-free layer in acetone using the polyethyleneimine (PEI) surfactant is first determined, and the effect of pre-sintering atmospheres (air and 5% H_2 bal Ar) on cyclic oxidation resistance at 800 °C for 500 h will be investigated.

2. Experimental

2.1 $NiFe_2O_4$ Spinel Synthesis

NiO (Sigma-Aldrich, Art No. 637130) and Fe_2O_3 (Merck, Art No.3924) powders were used as precursors for the synthesis of $NiFe_2O_4$ spinel by a solid state reaction. The NiO and Fe_2O_3 (1:1 ratio) were mixed in ethanol for 24 h. The slurry was then dried at 100 °C followed by calcination at 1100 °C for 3 h. Subsequently, the obtained powder was ball-milled in planetary mill (mill to powder 10:1) for 12 h. The XRD technique was then employed to characterize the synthesized $NiFe_2O_4$ spinel. The XRD pattern was recorded (Philips PW3710, Amsterdam, the Netherlands) using a Cu Kα monochromatized radiation source. Also, particles size distribution analysis was performed by monitoring the scattering of a laser beam by particles in a water stream (Particle size analyzer, Fritsch, Germany).

2.2 SUS 430 Treating

SUS 430, whose chemical composition has been determined by emission spectrometry (WAS, Germany) and presented in Table 1, was used as the interconnect substrate with $20 \times 20 \times 3$ (mm × mm × mm) dimensions. Prior to deposition, the substrate was gritted with SiC abrasive paper of #500 in order to remove the native oxide layer and cleaned with acetone in an ultrasonic bath for 20 min.

### 2.3 Suspension Preparation and EPD

1 g/L of $NiFe_2O_4$ homogeneous suspension was prepared in acetone by sonicating in an ultrasonic bath for 20 min. To provide a stable suspension for the EPD process, Polyethylene imine (Sigma-Aldrich, Art No: 101089605) was used as the dispersing agent. The conductivity of the as-prepared suspensions was measured using WTW-Inolab conductivity meter. The deposition experiments of $NiFe_2O_4$ particles in suspension were conducted using an EPD setup (Fig. 1b). A high-voltage DC power supply (PST1002) was used for the deposition of $NiFe_2O_4$ powder on SUS 430 electrodes at a distance of 1 cm. The deposition potential and duration were determined to be 100 and 300 V/cm and 1 min, respectively. The deposition pattern of the obtained layers was studied using optical microscope (OM, Olympus/BX61) and scanning electron microscope (SEM, WEGAII TESCAN). Also, quantitative analysis of the thickness of the obtained as-deposit layers was performed using a Veeco Dektak-3 profiler.

2.4 Pre-sintering and Oxidation of Coatings

The uncoated and $NiFe_2O_4$-coated SUS 430 samples were pre-sintered in air at 900 °C for 3 h, and then oxidized at 800 °C for 500 h. Also, to study the effect of pre-sintering atmosphere on the oxidation resistance, the pre-sintering of the coated and uncoated samples were performed in 5% H_2 bal Ar

Fig. 1 (a). A schematic illustration of planar SOFC stack (Ref 9). (b). The schematic of EPD setup

Table 1 Chemical composition (wt.%) of SUS 430

	wt.%		wt.%		wt.%
Fe	base	V	0.1	C	0.026
Cr	16.5	Si	0.31	W	<0.02
Mn	0.51	Mo	0.05	Ti	<0.001
Ni	0.16	S	<0.003	Nb	<0.003
Cu	0.12	Al	<0.001	Co	<0.002

Table 2 Sample specification and experimental procedure

Sample	Coating status	Pre-sintering atmosphere	Pre-sintering temperature, °C	Pre-sintering Time, h	Oxidation temperature, °C	Oxidation time, h
A	Uncoated	Air	900	3	800	500
B	$NiFe_2O_4$ -Coated	Air	900	3	800	500
C	Uncoated	$5H_2/Ar$	900	3	800	500
D	$NiFe_2O_4$ -Coated	$5H_2/Ar$	900	3	800	500
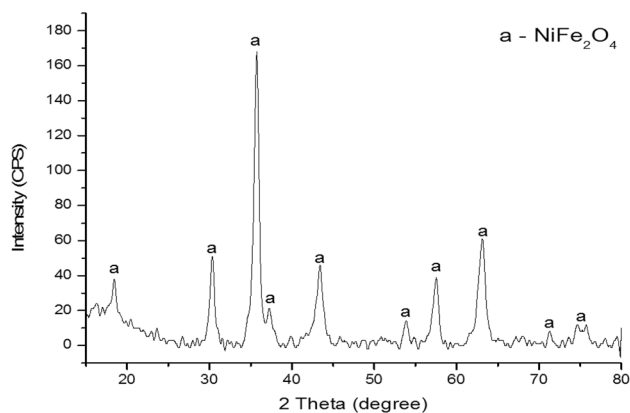
Fig. 2 X-ray diffraction pattern of $NiFe_2O_4$ spinel powder

Fig. 3 Particle size distribution of $NiFe_2O_4$ spinel

at 900 °C for 3 h followed by cyclic oxidation for 500 h at 800 °C in accordance with the operation temperature of SOFC cathode. Each cycle consisted of 50 h of heating in air and then cooling down to the room temperature. The various processing conditions of samples employed in this study are shown in Table 2.
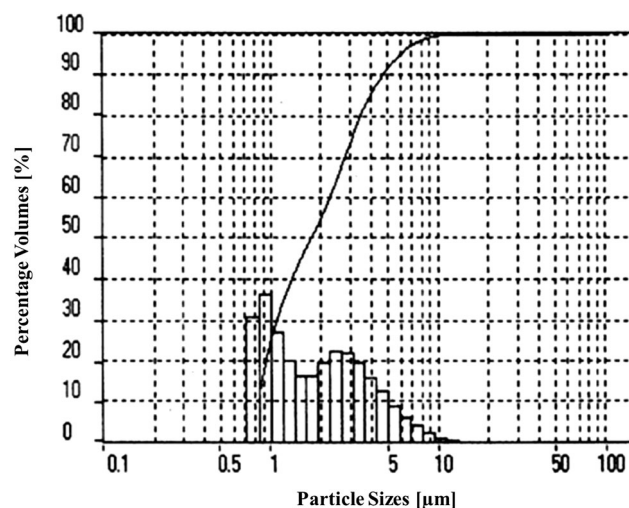
3. Results and Discussion

3.1 Synthesis of NiFe₂O₄ Spinel

The XRD pattern of $NiFe_2O_4$ spinel synthesized by the solid state reaction is shown in Fig. 2 where all peaks were identified as $NiFe_2O_4$ powder [(JCPDS card number: 044-1485). The particle size distribution of synthesized $NiFe_2O_4$ spinel used for EPD is shown in Fig. 3. This plot illustrates the count fractions of particle size versus the particle size diameter where the particle size diameter is less than 10 μm (D_{50} = 1.76 μm).

### 3.2 The Effect of Dispersing Agent on EPD Current and Conductivity

The $NiFe_2O_4$ powder was dispersed in acetone and sonicated for 20 min. Since the suspension was not stable enough without the addition of dispersant, one drop (12 μL) of polyethyleneimine (PEI) was used to increase the surface charge of the $NiFe_2O_4$ particles, enhancing the dispersing capability of the medium (Ref 41). The PEI addition was observed to increase suspension conductivity (3 μS/cm)

approximately 10 times in comparison to suspensions in which no additives had been used (0.3 μS/cm). The current density results during EPD versus deposition duration (Fig. 4) for $NiFe_2O_4$ suspension with (at 100 and 300 V) and without dispersant (300 V) indicate that the current density decreased with time for all experiments which is attributed to the formation of an insulating layer of $NiFe_2O_4$ particles (Ref 40). As demonstrated by the I-t graph in Fig. 4, higher voltages resulted in higher current densities for suspensions of the same amount of PEI which can be attributed to the evident increase in the driving force at higher potentials. The important point about the deposition carried out at 300 V in the presence of PEI is the higher current drop compared with depositions performed at 100 V with PEI and 300 V without PEI. Severe current drop in such conditions could be attributed to the formation of thicker layers resulting in higher resistance against current flow (Ref 40).

3.3 The Effect of Voltage on the Surface Morphology

Figure 5(a) and (b) shows the $NiFe_2O_4$ coating obtained by EPD from an acetone-based suspension for 1 min at 300 V with and without PEI dispersant, respectively. In this case, the deposition yield increased with the addition of PEI, and the coating was observed to be of sufficient adherence to the substrate. However, the coating was prone to poor adhesion in the absence of PEI. It is obvious that the spinel layer deposited
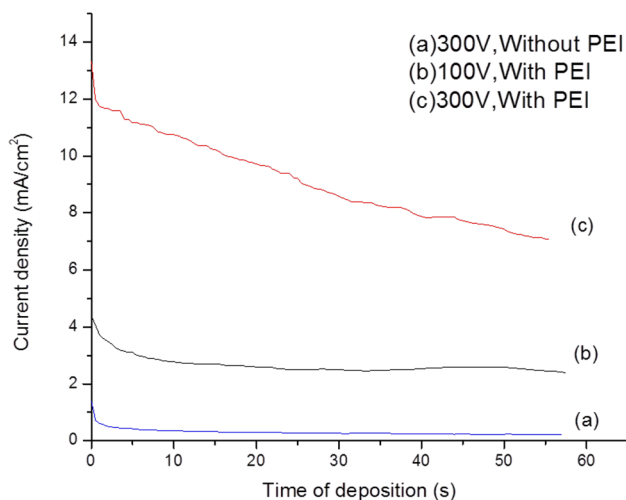
Fig. 4 Current density in EPD of NiFe$_2$O$_4$ with and without PEI at 100 and 300 V
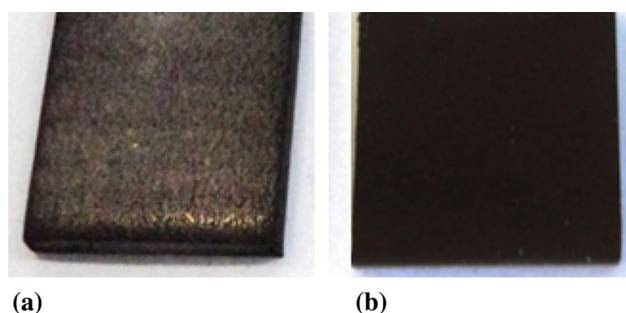
Fig. 5 NiFe$_2$O$_4$-coated SUS 430 at 300 V, Suspension without PEI (a) and with PEI (b)

from the dispersant-based suspension was more uniform than the one without the dispersing agent. The OM (a and b) and SEM (c and d) images of as NiFe$_2$O$_4$ spinel coatings deposited by EPD at electric fields of 100 and 300 V can be seen in Fig. 6. The thickness of the layer obtained in 100 V was approximately 20 μm. As shown in Fig. 6, the electrophoretically deposited layer in 300 V resulted in the formation of surface cracks, whereas in 100 V crack-free deposits were obtained which could be attributed to swift evaporation of the liquid (acetone) trapped within the layer (Ref 42, 43). The formation of particulate film on the electrode is a kinetic phenomenon and the applied field affects the deposition rate and the structure of the deposit. Although powders can be deposited more quickly if stronger electric fields up to 300 V are applied, high deposition rates can damage the quality of the resulting layer. High electric fields may cause turbulence across the suspension, giving rise to undesirable fluid flows during the deposition process. In addition, particles can move so fast that

they do not have enough time to find their best positions on the substrate to form a close-packed structure (Ref 40).

3.4 The Effect of Pre-sintering Atmosphere on Oxidation Resistance

As mentioned above, two different pre-sintering atmospheres have been used. The main goal of this heat treatment is to control the weight change and the oxidation resistance. Fig. 7 shows the weight changes of the uncoated and coated samples (crack-free layer in 100 V) as a function of oxidation time during the cyclic oxidation test. In this figure, curve (a) depicts the NiFe$_2$O$_4$-coated SUS 430 pre-sintered in air for 3 h at 900 °C followed by 500 h oxidation in air at 800 °C and curve (b) is related to the SUS 430 pre-sintered in air for 3 h at 900 °C followed by 500 h oxidation in air at 800 °C. Also, curve (a) and (b) in Fig. 8 represents the uncoated and NiFe$_2$O$_4$-coated SUS 430 pre-sintered in 5% H$_2$ bal Ar for 3 h at 900 °C followed by 500 h oxidation in air at 800 °C, respectively. According to the mentioned graphs (a and b graphs in Fig. 7), the weight gain of sample B (coated/air pre-sintered) is higher than that of the sample A (uncoated/air pre-sintered). It can be attributed to the tendency of the NiFe$_2$O$_4$ spinel to adsorb oxygen from air atmosphere. The surface morphologies of the samples A and B are shown in Fig. 9. As shown in Fig. 9(b), the surface of sample B is uniform and no spalling is observed on the surface. However, Fig. 9(a) clearly reveals the spalled areas on the surface of sample A. Hence, the oxide scale developed on the NiFe$_2$O$_4$-coated steel is evidently of a higher spallation resistance than that formed on the uncoated steel.

The slope of the curves in Fig. 7 and 8, after 50 h, was found to follow the Wagner theory defined as $(\Delta W/A)^2 = K_p\, t$, where ΔW is mass gain, A is the surface of samples, K_p is the oxidation parabolic rate constant, and t is the oxidation duration (Ref 44, 45). According to Fig. 7 and 8, the K_p values for B and D samples (coated) are 5.19×10^{-12} and 8.9×10^{-15} g^2 cm^{-4} s^{-1}, respectively. Also, the K_p values for sample A and C (uncoated) are 1.96×10^{-12} and 3.36×10^{-14} g^2 cm^{-4} s^{-1}, respectively. These results clearly indicate that sintering the sample in hydrogen-reducing atmosphere would decrease the parabolic oxidation rate constant 583 times stronger than sintering in air.

SEM/EDS analysis was employed to study the elemental oxidation products on the surface and along the cross section of tested samples. Cross-sectional image, EDS line scan, and EDS results of sample A (uncoated/air pre-sintered), shown in Fig. 10, reveal that the oxide layer consisted mainly of Cr, Fe, O, and a small amount of Mn. The remaining Au from the SEM sample preparation procedure was also detected. The EDS analysis of the A and B areas as shown in Fig. 10 shows that chromium was present in the steel and enriched in the oxide layer, with the amount of Cr in the inner oxide higher than in the outer oxide. Moreover, Fe was present in the steel but depleted in the oxide layer. Oxygen is also present in its oxide form and is depicted to increase as the Cr content is enhanced.
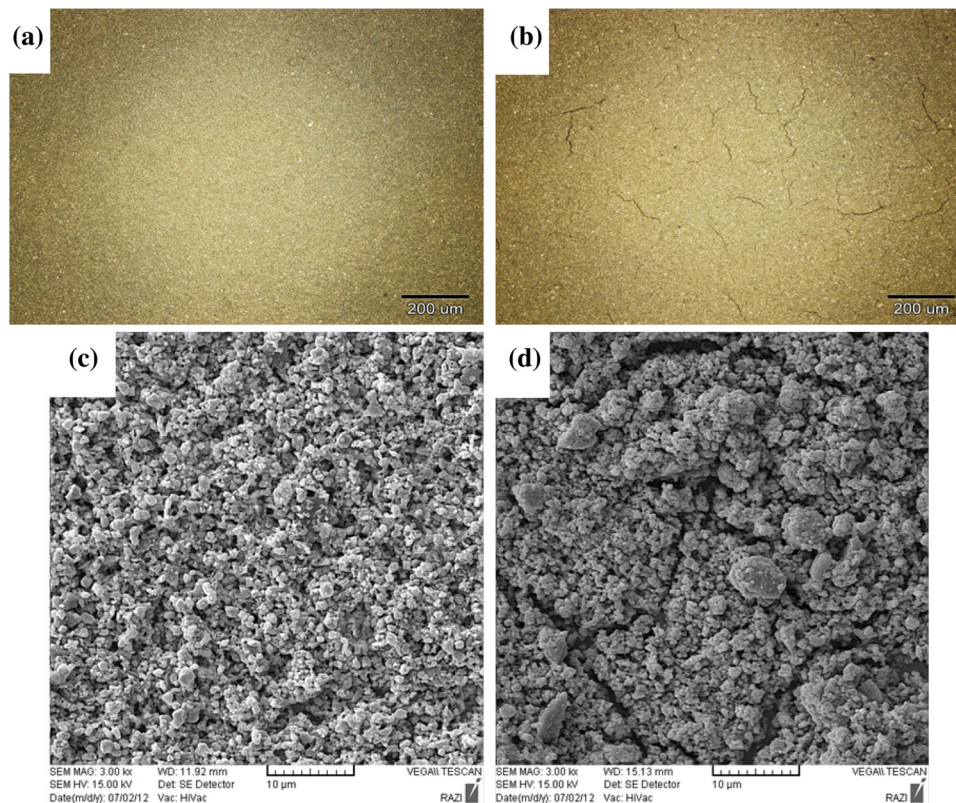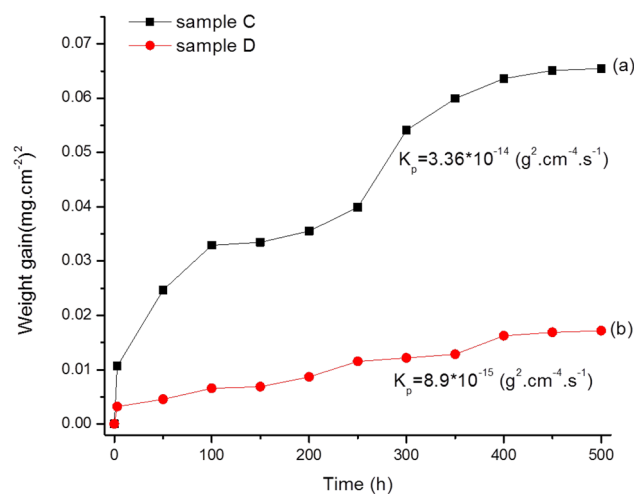
Fig. 6 The OM images (a: 100 V and b: 300 V) and SEM images (c: 100 V and d: 300 V) of the deposition patterns obtained by the EPD method for NiFe$_2$O$_4$ particles in acetone
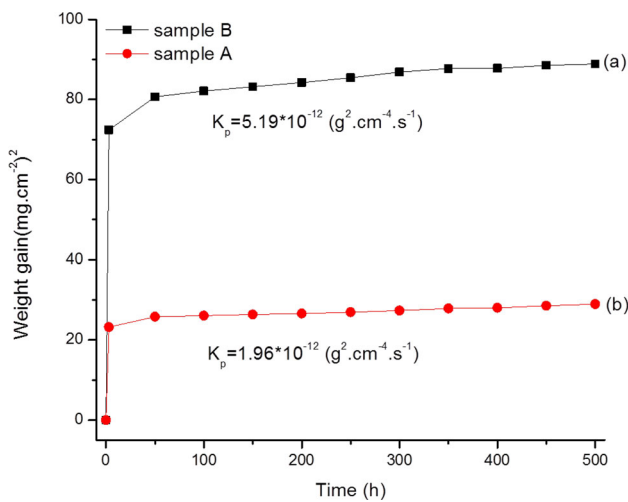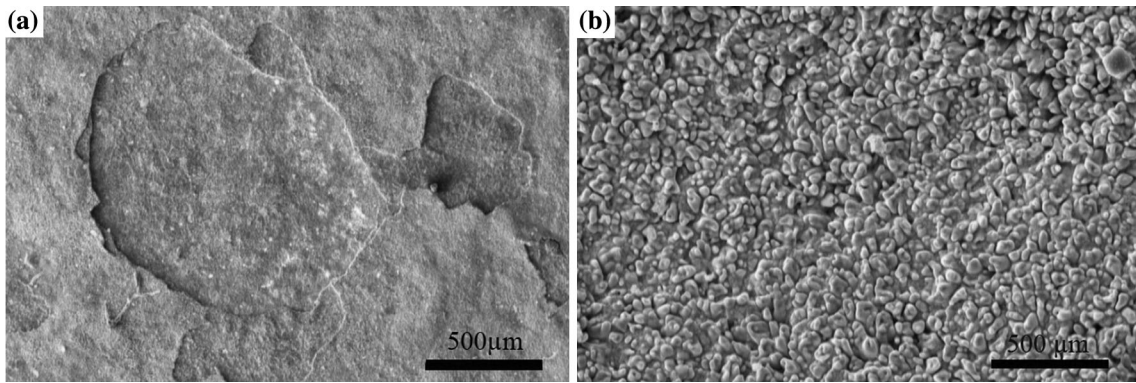

Fig. 7 Weight gains of sample A (uncoated/air pre-sintered) and B (coated/air pre-sintered)

Fig. 8 Weight gains of sample C (uncoated-5H$_2$/Ar pre-sintered) and D (coated-5H$_2$/Ar pre-sintered)

The cross-sectional SEM image of sample C (uncoated-5H$_2$/ Ar pre-sintered) is shown in Fig. 11. It is obvious that the average oxide scale is about 21 μm thick, while the thickness of the uniform oxide layer of sample A (uncoated/air pre-sintered)
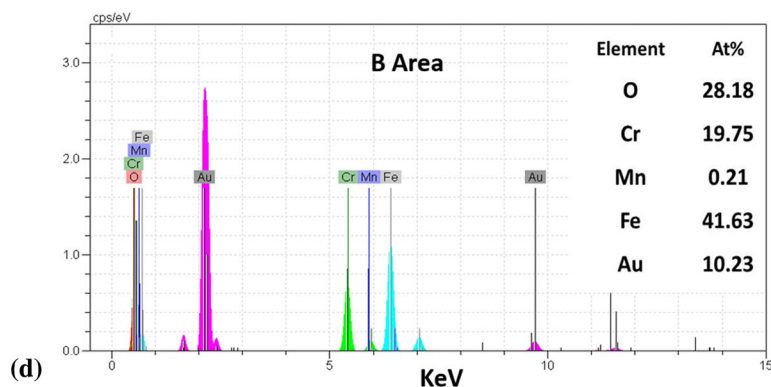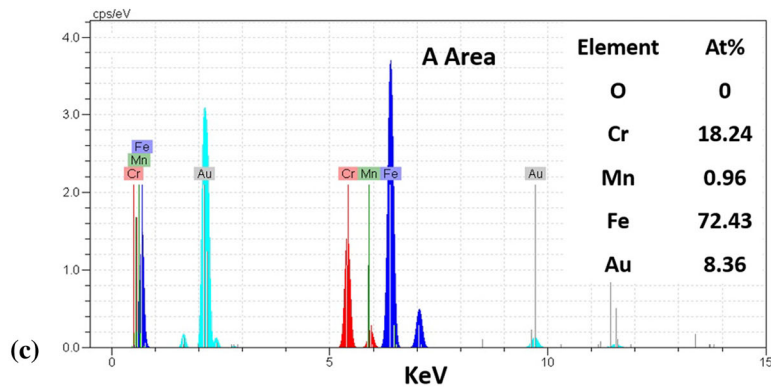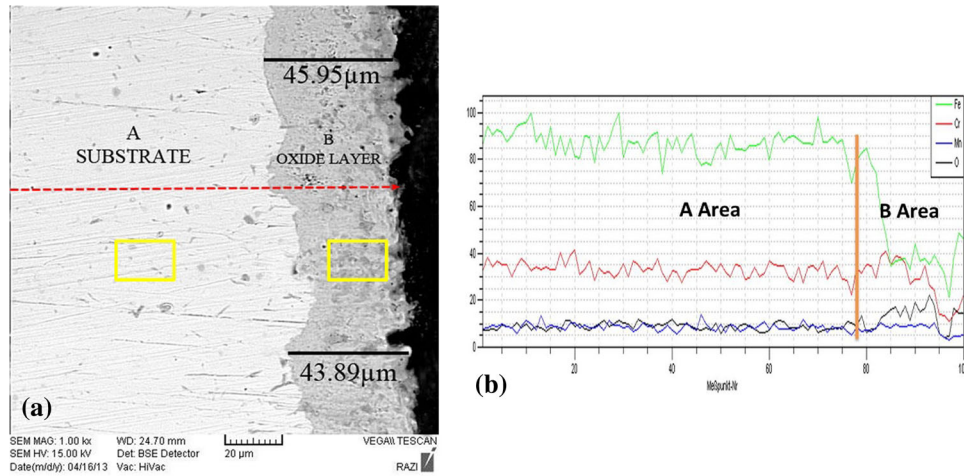
is ∼45 μm, as shown in Fig. 10(a). The higher oxide layer thickness of sample A compared with sample C can be attributed to oxygen diffusion from air atmosphere through the oxide layer in the pre-sintering stage. The oxidation

Fig. 9 The SEM image showing the surface morphology of sample A (a) (uncoated/air pre-sintered) and B (b) (coated/air pre-sintered)

Fig. 10 SEM cross section (a), (b) EDS line scan, (c) A area EDS analysis, and B area EDS analysis (d) of sample A (uncoated/air pre-sintered)
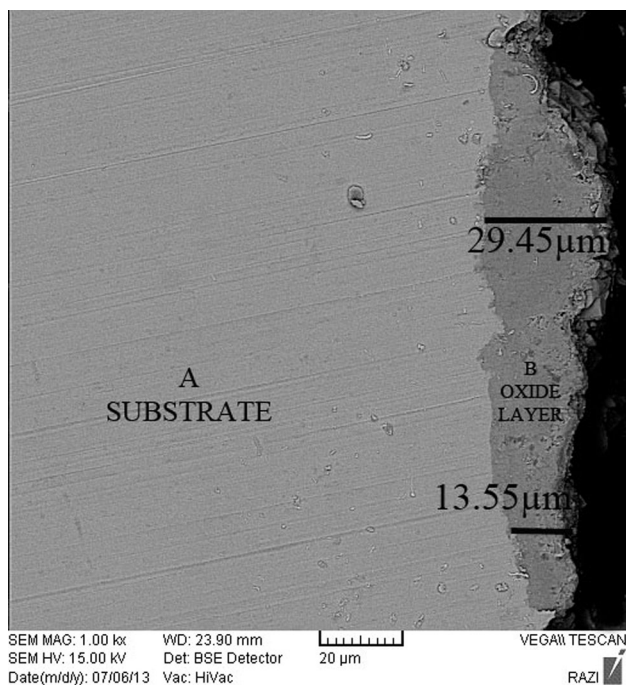
Fig. 11 SEM cross-sectional image of sample C (uncoated-5H₂/Ar pre-sintered)

phenomenon (Ref 15-17, 22-28, 37, 45-50) and its mechanisms (Ref 46, 51) for a typical metallic interconnect alloy in SOFC structure have been studied by many researchers under various experimental conditions. It has been reported that, normally, oxygen ions are chemisorbed on the metal surface and simultaneously outward Cr, Fe, and Mn main cations diffuse through the structural defects toward the oxide surface which results in the formation and growth of the oxide layer (Ref 46).

Figure 12 presents the EDS analysis results of oxide and coating layer, cross-sectional image, and EDS line scan of sample B (coated/air pre-sintered). It is obvious that three layers can be distinguished across the coated sample (Fig. 12a): coating layer, oxide layer, and the substrate. A suitable adhesion is observed between the coating and the substrate without cracking or delamination.

Since the coating layer is intended to simultaneously hinder Cr-volatility/diffusion into the surface and Fe and O diffusion into the substrate (SUS 430), the total oxide layer for the coated sample (Fig. 12a) grew less than that for the uncoated samples (Fig. 10a). The line scan indicates that (Fig. 12b) Cr is present in the steel and increases in region B, while severely decreasing along the oxidized layer (C Area). Thus, it can be concluded that after oxidizing the specimen for 500 h, migration of the chromium toward the NiFe₂O₄ coating layer was effectively reduced. To study the effect of pre-sintering atmosphere on the growth of the oxide layer, sample D (coated-5H₂/Ar pre-sintered) was also characterized. Figure 13 shows the cross-sectional SEM image, EDS line scan, and the EDS results. As illustrated in Fig. 13(a), the thickness of the whole oxide layer (∼7 μm) was thinner than that formed in sample B (coated/air pre-sintered) (∼30 μm). The green trace shows that the Cr content increases at the interface between the substrate and the coating. However, the Cr content is decreased along the coating layer.

The XRD analysis was used to identify the oxide scales formed during cyclic oxidation on the uncoated and NiFe₂O₄-spinel coated samples. The XRD analysis [Fig. 14—No. (2)] of sample A (uncoated/air pre-sintered) indicates that the sample contained chromium oxides and Fe₂O₃-based phases. However, sample D (coated-5H₂/Ar pre-sintered) [Fig. 14—No.(3)] shows characteristic Ni-Fe₂O₄, chromium oxides, Fe₂O₃, FeCr₂O₄, and NiCrO₄ phases. Inward oxygen, iron diffusion. and outward chromium cations diffusion toward the oxide surface/coating resulted in the formation of Ni/Cr and Fe/Cr oxide phases (Ref 36-38, 46, 52). Moreover, since the penetration depth of XRD is higher than the thick film thickness, the Fe-Cr phase was detected on the substrate.
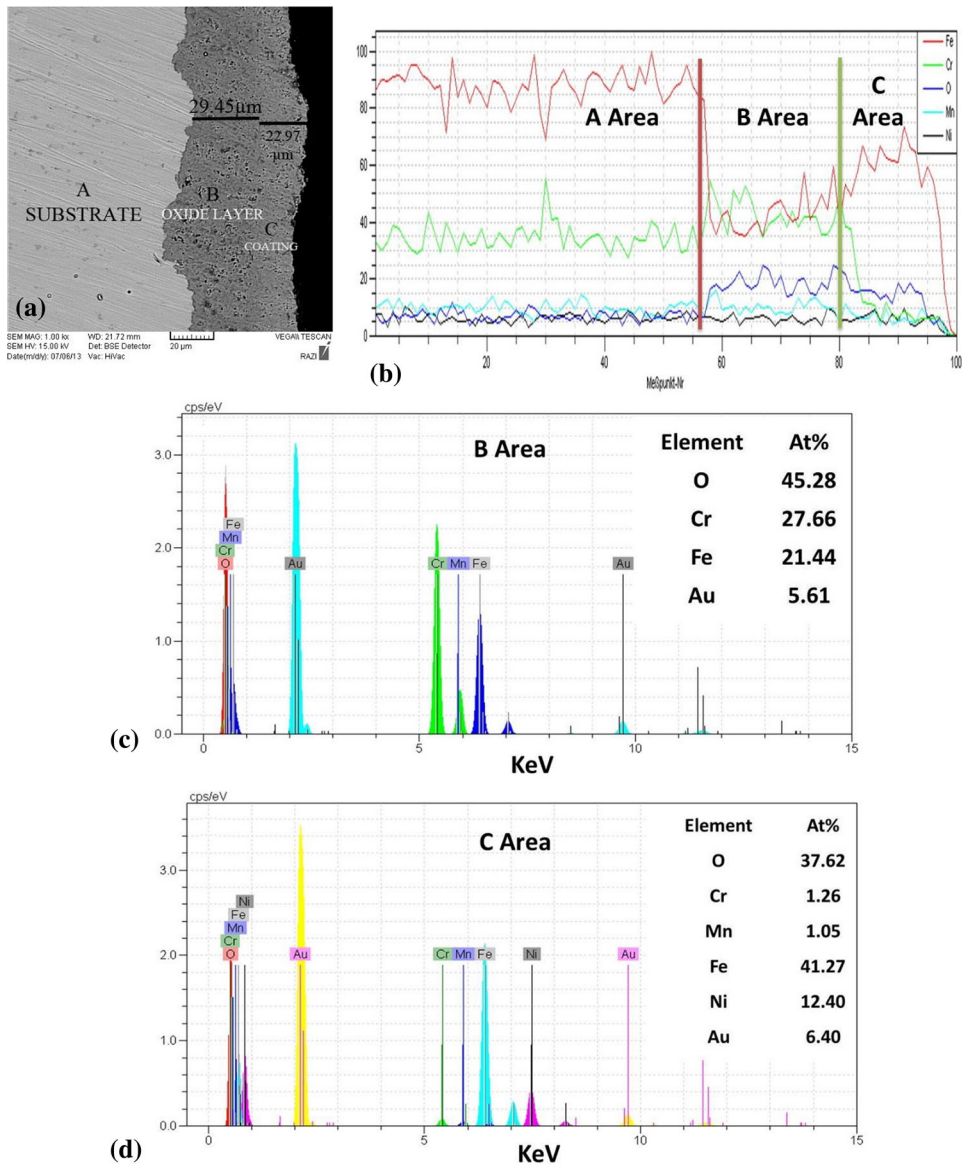
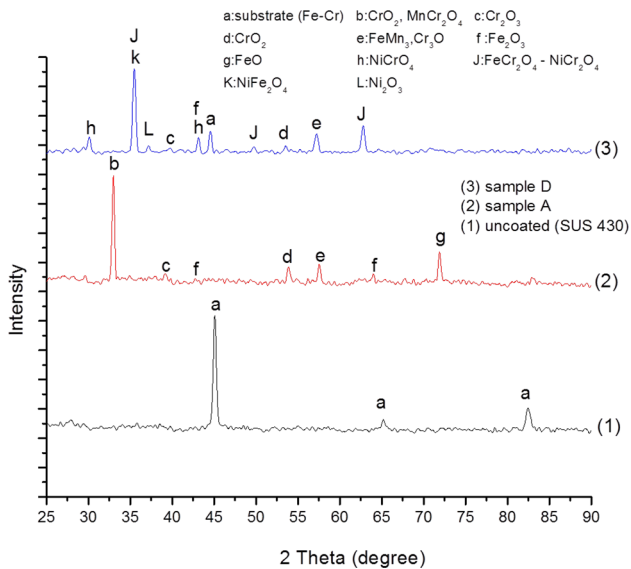**Fig. 12** SEM cross section (a), (b) EDS line scan, (c) A area EDS analysis, and B area EDS analysis (d) of sample B (uncoated/air pre-sintered)
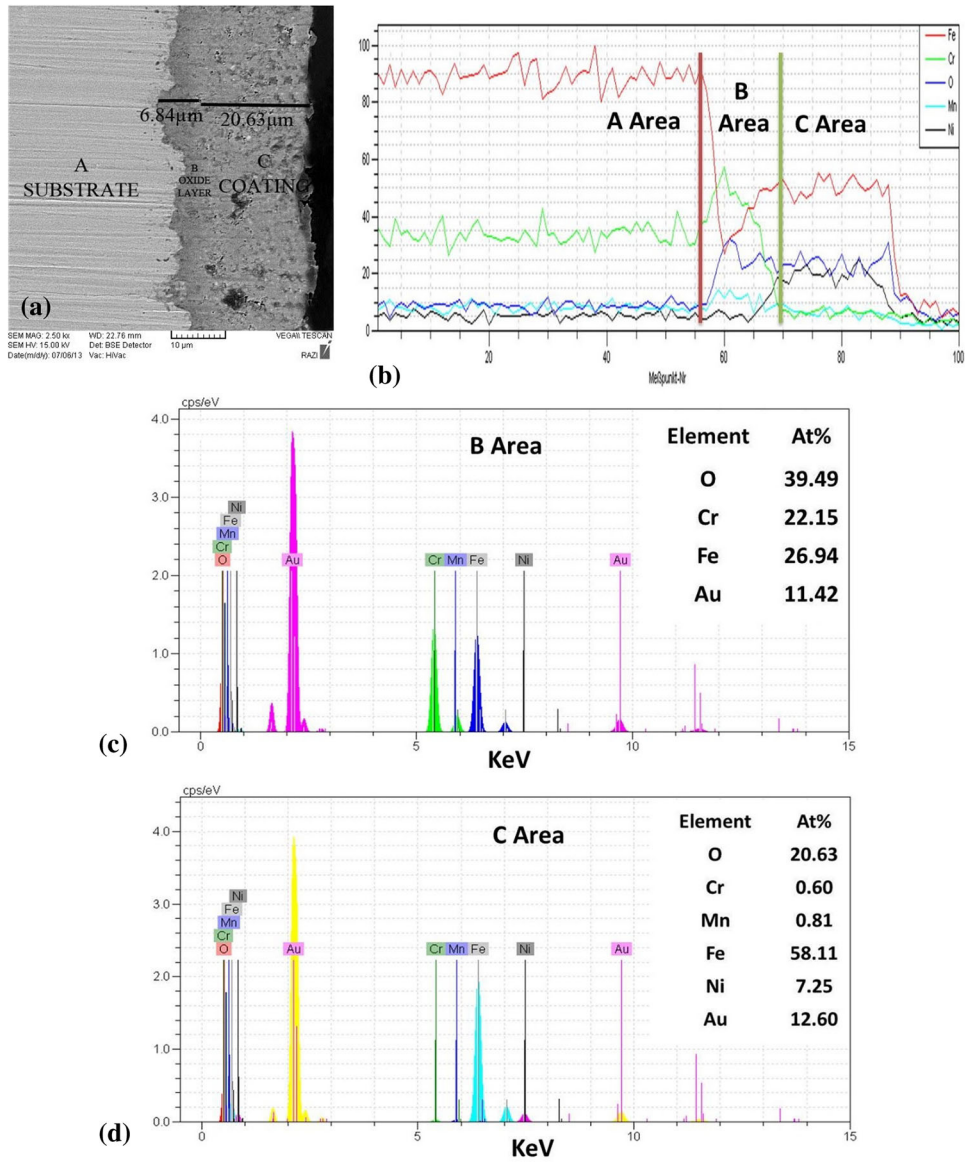
Fig. 13 SEM cross section (a), (b) EDS line scan, (c) A area EDS analysis, and B area EDS analysis (d) of sample D (coated-5H$_2$/Ar pre-sintered)

a:substrate (Fe-Cr) b:CrO$_2$, MnCr$_2$O$_4$ c:Cr$_2$O$_3$
d:CrO$_2$ e:FeMn$_3$,Cr$_3$O f :Fe$_2$O$_3$
g:FeO h:NiCrO$_4$ J:FeCr$_2$O$_4$ - NiCr$_2$O$_4$
K:NiFe$_2$O$_4$ L:Ni$_2$O$_3$

(3) sample D
(2) sample A
(1) uncoated (SUS 430)

Fig. 14 The XRD patterns of (1) sample A (uncoated/air pre-sintered) (2) sample B (coated/air pre-sintered) (3) sample D (coated-5H$_2$/Ar pre-sintered)

4. Conclusion

The pure NiFe$_2$O$_4$ spinel with particle size of less than 10 µm was synthesized by a solid state reaction. The spinel powder was then applied on SUS 430 ferritic stainless steel via EPD. The NiFe$_2$O$_4$ spinel coating acted as an effective barrier against chromium migration outward the substrate. Chromium atomic ratio within the surface of cyclic oxidized uncoated SUS 430 relative to air pre-sintered atmosphere and hydrogen pre-sintered ones was measured to be nearly 14- and 30-fold, respectively. The use of a reducing atmosphere before the oxidation of the coated samples had a significant effect on the oxidation behavior decreasing the oxidation rate constant (K_p) approximately 583 times compared with the air pre-sintered uncoated sample.

References

1. Mark C. Williams, Joseph P. Strakey, and Wayne A. Surdoval, The U.S. Department of Energy, Office of Fossil Energy Stationary Fuel Cell Program, *J. Power Sources*, 2005, **143**, p 191–196
2. Wei Zhou, Ran Ran, and Zongping Shao, Progress in Understanding and Development of Ba$_{0.5}$Sr$_{0.5}$Co$_{0.8}$Fe$_{0.2}$O$_{3-X}$-Based Cathodes for Intermediate-Temperature Solid-Oxide Fuel Cells: A Review, *J. Power Sources*, 2009, **192**(2), p 231–246
3. T. Brylewski, M. Nanko, T. Maruyama, and K. Przybylski, Application of Fe-16Cr Ferritic Alloy to Interconnector for a Solid Oxide Fuel Cell, *Solid State Ion.*, 2001, **143**(2), p 131–150
4. M.A. Callander, Material Issues for Fuel Cell Applications, *Mater. High Temp.*, 2007, **24**(3), p 197–203
5. Zhu Wz and Deevi Sc, Opportunity of Metallic Interconnects for Solid Oxide Fuel Cells: A Status on Contact Resistance, *Mater. Res. Bull.*, 2003, **38**(6), p 957–972
6. W.Z. Zhu and S.C. Deevi, Development of Interconnect Materials for Solid Oxide Fuel Cells, *Mater. Sci. Eng. A*, 2003, **348**(1-2), p 227–243
7. Maria Jose Garcia-Vargas, Laurent Lelait, Vladislav Kolarik, Harald Fietzek, and Maria del Mar Juez-Lorenzo, Oxidation of Potential SOFC Interconnect Materials, Crofer 22 APU and Avesta 353 MA, in Dry and Humid Air Studied In Situ by X-ray Diffraction, *Mater. High Temp.*, 2005, **22**(3-4), p 245–251
8. J. Yoo, S.-K. Woo, J.H. Yu, S. Lee, and G.W. Park, La$_{0.8}$Sr$_{0.2}$MnO$_3$ and (Mn$_{1.5}$Co$_{1.5}$) O$_4$ Double Layer Coated by Electrophoretic Deposition on Crofer22 APU for SOEC Interconnect Applications, *Int. J. Hydrog. Energy*, 2009, **34**(3), p 1542–1547
9. K. Lai et al., A Quasi-Two-Dimensional Electrochemistry Modeling Tool for Planar Solid Oxide Fuel Cell Stacks, *J. Power Sources*, 2011, **196**(6), p 3204–3222
10. J. Wu and X. Liu, Recent Development of SOFC Metallic Interconnect, *J. Mater. Sci. Technol.*, 2010, **26**(4), p 293–305
11. L.G.P. Andre, Cologna Marco, Sglavo Vincenzo, and Raj Rishi, Flash-Sintering of Co$_2$MnO$_4$ Spinel for Solid Oxide Fuel Cell Applications, *J. Power Sources*, 2011, **196**, p 2061–2065
12. Cezarina C. Mardare, Henrik Asteman, Michael Spiegel, Alan Savan, and Alfred Ludwig, Investigation of thermally oxidized Mn-Co thin films for application in SOFC metallic interconnects, *Appl. Surf. Sci.*, 2008, **255**, p 1850–1859
13. N. Shaigan, W. Qu, Dg Ivey, and W. Chen, A Review of Recent Progress in Coatings, Surface Modifications and Alloy Developments for Solid Oxide Fuel Cell Ferritic Stainless Steel Interconnects, *J. Power Sources*, 2010, **195**(6), p 1529–1542
14. R. Gordon et al., Dual-Environment Effects on the Oxidation of Metallic Interconnects, *J. Mater. Eng. Perform.*, 2006, **15**(4), p 404–409
15. Z. Yang, K.S. Weil, D.M. Paxton, and J.W. Stevenson, Selection and Evaluation of Heat-Resistant Alloys for SOFC Interconnect Applications, *J. Electrochem. Soc.*, 2003, **150**(9), p 1188–1201
16. S. Elangovan et al., Evaluation of Ferritic Stainless Steel for Use as Metal Interconnects for Solid Oxide Fuel Cells, *J. Mater. Eng. Perform.*, 2004, **13**(3), p 265–273
17. Z. Yang et al. (Mn, Co)$_3$O$_4$ Spinel Coatings on Ferritic Stainless Steels for SOFC Interconnect Applications, *Int. J. Hydrog. Energy*, 2007, **32**(16), p 3648–3654
18. J.W. Fergus, Metallic Interconnects for Solid Oxide Fuel Cells, *Mater. Sci. Eng. A*, 2005, **397**(1-2), p 271–283
19. S. Geng, J. Zhu, M.P. Brady, H.U. Anderson, X.-D. Zhou, and Z. Yang, A Low-Cr Metallic Interconnect for Intermediate-Temperature Solid Oxide Fuel Cells, *J. Power Sources*, 2007, **172**(2), p 775–781
20. Z. Yang, G. Xia, P. Singh, and J.W. Stevenson, Electrical Contacts Between Cathodes and Metallic Interconnects in Solid Oxide Fuel Cells, *J. Power Sources*, 2006, **155**(2), p 246–252
21. M. Krumpelt, T. Kaun, T.A. Cruse, M.C. Hash. "SOFC Research and Development." Office of Fossil Energy Fuel Cell Program. Annual Report (2004)
22. A.M. Dayaghi et al., Pre-Treatment and Oxidation Behavior of Sol-Gel Co Coating on 430 Steel in 750 °C Air with Thermal Cycling, *Surf. Coat. Technol.*, 2012, **206**(16), p 3495–3500
23. R. Lacey et al., Evaluation of Co and Perovskite Cr-Blocking Thin Films on SOFC Interconnects, *Solid State Ionics.*, 2010, **181**(27-28), p 1294–1302
24. H. Kurokawa et al., Chromium Vaporization of Bare and of Coated Iron-Chromium Alloys at 1073 K, *Solid State Ionics.*, 2007, **178**(3-4), p 287–296
25. J.W. Fergus, Synergism in the Design of Interconnect Alloy-Coating Combinations Solid for Oxide Fuel Cells, *Scr. Mater. A.*, 2011, **65**(2), p 73–77
26. J. Wu et al., The Performance of Solid Oxide Fuel Cells with Mn-Co Electroplated Interconnects as Cathode Current Collector, *J. Power Sources.*, 2009, **189**(2), p 1106–1113
27. N. Shaigan et al., Co/LaCrO$_3$ Composite Coatings for AISI, 430 Stainless Steel Solid Oxide Fuel Cell Interconnects, *J. Power Sources.*, 2008, **185**(1), p 331–337
28. X. Deng et al., Cobalt Plating of High Temperature Stainless Steel Interconnects, *J. Power Sources.*, 2006, **160**(2), p 1225–1229
29. J. Froitzheim et al., Long Term Study of Cr Evaporation and High Temperature Corrosion Behaviour of Co Coated Ferritic Steel for Solid Oxide Fuel Cell Interconnects, *J. Power Sources.*, 2012, **220**, p 217–227

30. M. Palcut et al., Efficient Dual Layer Interconnect Coating for High Temperature Electrochemical Devices, *Int. J. Hydrogen Energy.*, 2012, **37**(19), p 14501–14510

31. J. Wu et al., Investigation of Mn/Co Coated T441 Alloy as SOFC Interconnect by On-Cell Tests, *Int. J. Hydrogen Energy.*, 2011, **36**(7), p 4525–4529

32. Å.H. Persson et al., Interaction Mechanisms Between Slurry Coatings and Solid Oxide Fuel Cell Interconnect Alloys During High Temperature Oxidation, *J Alloys Compd.*, 2012, **521**, p 16–29

33. A. Petric and H. Ling, Electrical Conductivity and Thermal Expansion of Spinels at Elevated Temperatures, *J. Am. Ceram. Soc.*, 2007, **90**, p 1515–1520

34. C.C. Mardare, H. Asteman, M. Spiegel, A. Savan, and A. Ludwig, Investigation of Thermally Oxidised Mn-Co Thin Films for Application in SOFC Metallic Interconnects, *Appl. Surf. Sci.*, 2008, **255**, p 1850–1859

35. B. Hua, W. Zhang, J. Wu, J. Pu, B. Chi, and L. Jian, A Promising NiCo$_2$O$_4$ Protective Coating for Metallic Interconnects of Solid Oxide Fuel Cells, *J. Power Sources.*, 2010, **195**(21), p 7375–7379

36. Y. Liu and D.Y. Chen, Protective Coatings for Cr$_2$O$_3$-Forming Interconnects of Solid Oxide Fuel Cells, *Int. J. Hydrogen Energy.*, 2009, **34**(22), p 9220–9226

37. S. Geng, S. Qi, Q. Zhao, S. Zhu, and F. Wang, Electroplated Ni-Fe$_2$O$_3$ Composite Coating for Solid Oxide Fuel Cell Interconnect Application, *Int. J. Hydrogen Energy.*, 2012, **37**(14), p 10850–10856

38. S. Geng, Q. Wang, W. Wang, S. Zhu, and F. Wang, Sputtered Ni Coating on Ferritic Stainless Steel for Solid Oxide Fuel Cell Interconnect Application, *Int. J. Hydrogen Energy.*, 2012, **37**(1), p 916–920

39. C. Kaya, F. Kaya, B. Su, B. Thomas, and A.R. Boccaccini, Structural and Functional Thick Ceramic Coatings by Electrophoretic Deposition, *Surf. Coat. Technol.*, 2005, **191**(2-3), p 303–310

40. L. Besra and M. Liu, A Review on Fundamentals and Applications of Electrophoretic Deposition (EPD), *Prog. Mater. Sci.*, 2007, **52**(1), p 1–61

41. F. Tang, T. Uchikoshi, K. Ozawa, and Y. Sakka, Effect of Poly Ethylene Imine on the Dispersion and Electrophoretic Deposition of Nano-Sized Titania Aqueous Suspensions, *J. Eur. Ceram. Soc.*, 2006, **26**, p 1555–1560

42. C.C. Chen, C.S. Jwo, and T.P. Teng, Decomposition of Formaldehyde by EPD Photo Catalyst Filters in HVAC, *Particuology.*, 2011, **9**(5), p 497–501

43. A.A. Sadeghi, T. Ebadzadeh, B. Raissi, S. Ghashghaie, and S.M.A. Fateminia, Application of the Multi-Step EPD Technique to Fabricate Thick TiO$_2$ Layers: Effect of Organic Medium Viscosity on the Layer Microstructure, *J. Phys. Chem. B.*, 2013, **117**(6), p 1731–1737

44. W.J. Quadakkers, J. Piron-Abellan, V. Shemet, and L. Singheiser, Metallic Interconnectors for Solid Oxide Fuel Cells: A Review, *Mater. High Temp.*, 2003, **20**, p 115

45. C. Wagner, *Z. Phys. Chem. B*, 1933, **21**, p 42

46. W. Qu et al., Yttrium, Cobalt and Yttrium/Cobalt Oxide Coatings on Ferritic Stainless Steels for SOFC Interconnects, *J. Power Sources.*, 2006, **157**(1), p 335–350

47. H. Ebrahimifar and M. Zandrahimi, Oxidation and Electrical Behavior of AISI, 430 Coated with Cobalt Spinels for SOFC Interconnect Applications, *Surf. Coat. Technol.*, 2011, **206**(1), p 75–81

48. B. Hua et al., Cyclic oxidation of Mn-Co spinel coated SUS 430 alloy in the cathodic atmosphere of solid oxide fuel cells, *Journal of Power Sources.*, 2008, **185**(1), p 419–422

49. W. Wei et al., Oxidation Resistance and Electrical Properties of Anodically Electrodeposited Mn-Co Oxide Coatings for Solid Oxide Fuel Cell Interconnect Applications, *J. Power Sources.*, 2009, **186**(2), p 428–434

50. X. Chen et al., Protective Coatings on Stainless Steel Interconnect for SOFCs: Oxidation Kinetics and Electrical Properties, *Solid State Ionics.*, 2005, **176**(5-6), p 425–433

51. P. Jian et al., Oxidation Kinetics and Phase Evolution of a Fe-16Cr Alloy in Simulated SOFC Cathode Atmosphere, *J. Power Sources.*, 2006, **158**(1), p 354–360

52. S. Geng et al., Evaluation of Electrodeposited Fe-Ni Alloy on Ferritic Stainless Steel Solid Oxide Fuel Cell Interconnect, *J. Power Sources.*, 2010, **195**(10), p 3256–3260